ORIGINAL RESEARCH

Open Access

Positronium lifetime validation measurements using a long-axial field-of-view positron emission tomography scanner

William M. Steinberger[1]*, Lorenzo Mercolli[2], Johannes Breuer[3], Hasan Sari[4], Szymon Parzych[5], Szymon Niedzwiecki[5], Gabriela Lapkiewicz[5], Pawel Moskal[5], Ewa Stepien[5], Axel Rominger[2], Kuangyu Shi[2] and Maurizio Conti[1]

*Correspondence:
william.steinberger@siemens-healthineers.com

[1] Siemens Medical Solutions USA, Inc., Knoxville, TN 37932, USA
[2] Department of Nuclear Medicine, Inselspital, Bern University Hospital, University of Bern, Bern, Switzerland
[3] Siemens Healthineers AG, Forchheim, Germany
[4] Siemens Healthineers International AG, Zurich, Switzerland
[5] Center for Theranostics, Institute of Physics, Jagiellonian University, ul. Lojasiewicza 11, 30-348 Krakow, Poland

Abstract

Background: Positron emission tomography (PET) traditionally uses coincident annihilation photons emitted from a positron interacting with an electron to localize cancer within the body. The formation of positronium (Ps), a bonded electron-positron pair, has not been utilized in clinical applications of PET due to the need to detect either the emission of a prompt gamma ray or the decay of higher-order coincident events. Assessment of the lifetime of the formed Ps, however, can potentially yield additional diagnostic information of the surrounding tissue because Ps properties vary due to void size and molecular composition. To assess the feasibility of measuring Ps lifetimes with a PET scanner, experiments were performed in a Biograph Vision Quadra (Siemens Healthineers). Quadra is a long-axial field-of-view (LA-FOV) PET scanner capable of producing list-mode data from single interaction events.

Results: Ortho-Ps (o-Ps) lifetimes were measured for quartz-glass and polycarbonate samples using a ^{22}Na positron source. Results produced o-Ps lifetimes of 1.538 ± 0.036 ns for the quartz glass and 1.927 ± 0.042 ns for the polycarbonate. Both o-Ps lifetimes were determined using a double-exponential fit to the time-difference distribution between the emission of a prompt gamma ray and the annihilation of the correlated positron. The measured values match within a single standard deviation of previously published results. The quartz-glass samples were additional measured with ^{82}Rb, ^{68}Ga and ^{124}I to validate the lifetime using clinically available sources. A double-exponential fit was initially chosen as a similar methodology to previously published works, however, an exponentially-modified Gaussian distribution fit to each lifetime more-accurately models the data. A Bayesian method was used to estimate the variables of the fit and o-Ps lifetime results are reported using this methodology for the three clinical isotopes: 1.59 ± 0.03 ns for ^{82}Rb, 1.58 ± 0.07 ns for ^{68}Ga and 1.62 ± 0.01 ns for ^{124}I. The impact of scatter and attenuation on the o-Ps lifetime was also assessed by analyzing a water-filled uniform cylinder ($20\,\phi \times 30$ cm^3) with an added ^{82}Rb solution. Lifetimes were extracted for various regions of the cylinder and while there is a shape difference in the lifetime due to scatter, the extracted o-Ps lifetime of the water, 1.815 ± 0.013 ns, agrees with previously published results.

Conclusion: Overall, the methodology presented in this manuscript demonstrates the repeatability of Ps lifetime measurements with clinically available isotopes in a commercially-available LA-FOV PET scanner. This validation work lays the foundation for future in-vivo patient scans with Quadra.

Keywords: Positronium imaging, Positron emission tomography, Molecular imaging

Background

Positronium (Ps) is a semi-stable hydrogen-like atom composed of a bonded positron-electron pair [1]. The spin states of the bonded pair determine the lifetime of the Ps. The ground state (1^1S_0), para-Ps (p-Ps), and triplet state (1^3S_1), ortho-Ps (o-Ps), of Ps have lifetimes of 125 ps and 143 ns respectively in a vacuum. Typically in solid or liquid materials the lifetime of o-Ps is on the order of 1-3 ns [1] due to pick-off processes that make the o-Ps lifetime dependent on the composition and void structure of the surrounding material [2–7]. This dependence of the o-Ps lifetime on surrounding material has piqued interest for applying o-Ps lifetime analysis to positron emission tomography (PET) to gain additional diagnostic information [8–16]. In-vivo measurements of patients are starting to be conducted with research scanners such as the J-PET, which has produced the first in-vivo patient Ps images [17]. Traditional PET scans reconstruct coincident annihilation photons emitted by the annihilation of a positron with an electron to isolate regions of significant uptake within the body. Ps formation can be detected by processing higher-order events. The two primary methods for measuring the Ps lifetime are as follows: the lifetime can be directly measured by using the emission of a prompt gamma ray as a start time [10–12, 18] or the ratio of 3γ events from the decay of o-Ps to 2γ events can be measured to infer the o-Ps lifetime [9, 18–20]. Measuring the o-Ps lifetime can yield additional diagnostic information such as tumor hypoxia [9, 12, 21] or the identification of diseased tissue [13, 19]. It is therefore the goal of this publication to validate the methodology for detecting and measuring o-Ps lifetimes within a Biograph Vision Quadra (Siemens Healthineers) (Quadra) scanner so that in-vivo human measurements can yield trusted results.

Recent advances in the acquisition architecture of the Quadra [22] have made it possible to isolate and analyze higher order coincident events in PET scans. List-mode data composed of single interactions within a block can be acquired and processed to measure triple-coincidence events. To test the viability of measuring the lifetime of positronium using a Quadra scanner, an experiment was performed similar to that presented and published by Takyu et al. [16, 23]. Quartz-glass and polycarbonate samples were acquired and Ps lifetimes were measured using two ^{22}Na positrons sources. The prompt gamma rays emitted by ^{22}Na were tagged as a "start" interaction and the subsequent detection of two annihilation photons were set as the "stop" interaction. The time differences between the emission of the prompt gamma rays and the annihilation of the positron were histogrammed to generate a time-difference spectrum and extract the o-Ps lifetime.

The predominant source used in laboratory settings to measure o-Ps lifetimes has been ^{22}Na. This source is commonly used because it decays with a 99.9 % probability of emitting a 1275 keV prompt gamma ray, has an end-point positron energy of 546 keV and it has a half life of 2.602 years. It was an additional goal of this work, however,

to demonstrate Ps lifetime measurements with clinically available sources that emit a prompt gamma ray such as ^{68}Ga, ^{82}Rb and ^{124}I. ^{68}Ga is used for detecting neuroendocrine tumors and prostate-specific membrane antigen scans, and has the following properties: a 67.8 min half life, 3.23 % emission of a 1077.3 keV prompt gamma ray, and a coincident positron end-point energy of 1899 keV. ^{82}Rb is used for myocardial perfusion, and has the following properties: a 75.5 s half life, 13 % emission of a 776.5 keV prompt gamma ray, and a coincident positron end-point energy of 2603 keV. ^{124}I is used for thyroid cancer or neuroblastoma (when labelled with metaiodobenzylguanidine), and has the following properties: a 4.18 day half life, 62.3 % emission of a 602.7 keV prompt gamma ray, and two dominant positron end-point energies of 1535 and 2138 keV. The higher energy positron emitted by ^{124}I, however, is not emitted with a prompt gamma ray. To validate the use of each of these clinical isotopes for measuring Ps lifetimes, experiments were performed where drops of the radiotracer in solution were placed on a known quartz-glass sample. The sample was measured and results were analyzed.

The aforementioned quartz-glass and polycarbonate samples do not contribute a significant amount of scatter or attenuation to the measurement. To assess how these parameters impact the resulting shape of the time-difference distribution and the resulting o-Ps lifetime, a uniform cylinder filled with water and a solution of ^{82}Rb was measured. Results were processed and subdivided into three regions of the uniform cylinder with volumes centered in the cylinder of ($5 \phi \times 15$ cm^3), ($10 \phi \times 20$ cm^3) and ($15 \phi \times 25$ cm^3). The lifetimes extracted from each region were directly compared with each other and the quartz-glass lifetime. It should be noted that there is no scatter, attenuation or normalization correction applied to the presented results. The following details the methodology used to obtain the resulting time-difference spectra and o-Ps lifetimes.

Methods

Sorting triple events

List-mode data were sorted, processed and energy qualified to isolate triple-coincident events from the data. Figure 1 shows a diagram depicting nine interactions occurring over time with coincidence windows following each event. The methodology used to define the number of coincidences selects all combination of triple events within a given coincidence window such that the series of events depicted in Fig. 1 would generate five triple events of the following combinations: (1-2-3), (2-3-4), (6-7-8), (6-8-9) and (7-8-9). This methodology
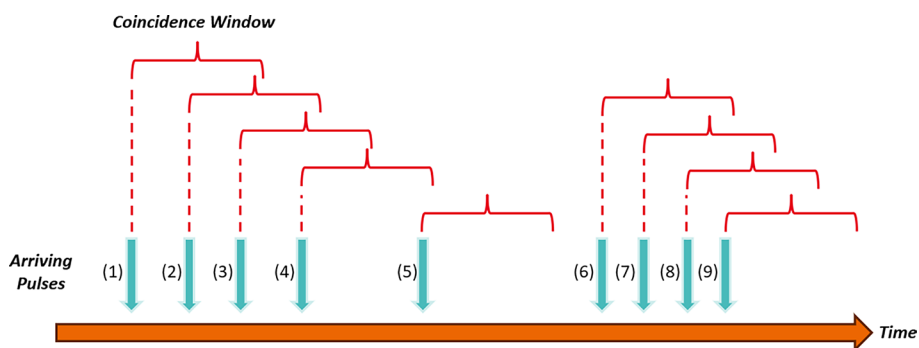
Fig. 1 Diagram depicting a series of single interactions with coincidence windows

was applied to events containing up to seven interactions within a given coincidence window.

The triple coincident events are then energy qualified such that two of the events are within a specified annihilation-photon energy window and one of the events is within a specified prompt gamma-ray energy window. Figure 2 shows the energy spectra for triple-coincident events within a 20 ns coincidence window for the quartz-glass measurement containing ^{124}I. The annihilation window was set to 460–545 keV and the prompt gamma-ray energy window was set to 568–639 keV. It should be noted in Fig. 2 that the first photon interaction is more likely to be within the prompt gamma-ray energy window. This result is intuitive since the prompt gamma ray is generally emitted well before the annihilation of the positron. For all other sources, an energy window of 435–585 keV was used for the annihilation photons. The energy spectrum has a maximum value of about 726 keV, and this final value in the spectrum is an integrating bin. This final bin contains energy information up to about 950 keV. For the ^{22}Na and ^{68}Ga measurements, the prompt gamma-ray energy window was set to 720–950 keV. The prompt gamma-ray energy window was set to 685–950 keV for the ^{82}Rb measurement. Once the interactions are energy qualified, an additional coincidence window of 4.2 ns was applied to the time difference between the annihilation photons.

Histo-imaging and time-difference calculations

The triple-interaction events that fall within the two coincidence time-window thresholds and pass energy qualification are reconstructed through a direct TOF reconstruction. All oblique angles and ring differences were accepted for this analysis. Figure 3 shows a depiction of a triple-interaction that meets the previously detailed energy and time requirements.

The distance between the two annihilation photons,

$$d = \|\vec{x}_1 - \vec{x}_0\|, \tag{1}$$

is calculated from the two interaction locations as depicted in Fig. 3. This distance is used to determine a TOF distance as described by
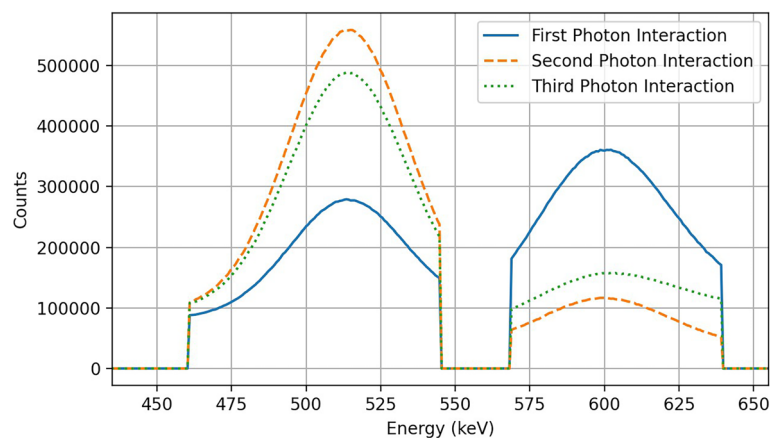
Fig. 2 Time-sorted and energy qualified spectra of triple events for the quartz-glass measurement containing approximately 4.7 MBq of ^{124}I in the FOV with energy windows of 460–545 keV for the annihilation photons and 568–639 keV for the prompt gamma ray
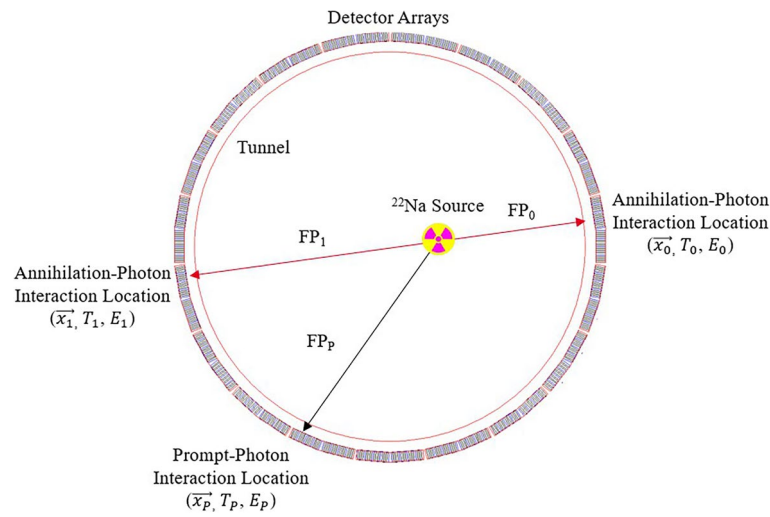
Fig. 3 Diagram depicting a triple-interaction event composed of a prompt gamma ray and two annihilation photons

$$d_t = d - \left(\frac{d}{2} + \frac{\Delta T c}{2} \right). \tag{2}$$

Within Eq. (2), ΔT is the time difference between the annihilation photons and c is the speed of light. The ratio of these two distance values are used to calculate the annihilation location of the positron, $\vec{x_{TOF}}$, as detailed in

$$\vec{x_{TOF}} = \left(1 - \frac{d_t}{d} \right) \vec{x_0} + \frac{d_t}{d} \vec{x_1}. \tag{3}$$

The annihilation location, $\vec{x_{TOF}}$, can then be used to calculate the various flight paths, FP, for the annihilation photons and prompt gamma ray. Then the time difference between the emission of the prompt gamma ray and the annihilation of the positron can be calculated by

$$\Delta T_{Ps} = \left(T_{0/1} - \frac{FP_{0/1}}{c} \right) - \left(T_P - \frac{FP_P}{c} \right). \tag{4}$$

These positronium time-difference values are histogrammed to generate a time-difference distribution (TDD) or spectrum, which can be used to extract positronium lifetime information. It was found that using T_0 or T_1 in Eq. (4) with their respective flight path, FP, made no difference in the resulting TDD. Taking the average between the annihilation time, $\left(T_{0/1} - \frac{FP_{0/1}}{c} \right)$, calculated by both photons also made no difference in the resulting TDDs.

Accounting for ¹⁷⁶Lu background

Applying the initial methodology detailed in the previous two subsections to a uniform cylinder containing a ⁸²Rb solution produced a time-difference distribution with a spike at $\Delta T_{Ps} = 0$. To isolate the origin of this spike, a uniform cylinder ($20\,\phi \times 30\,\mathrm{cm}^3$) filled with 16.3 MBq of ¹⁸F was measured. Figure 4 shows the histo-image of the uniform
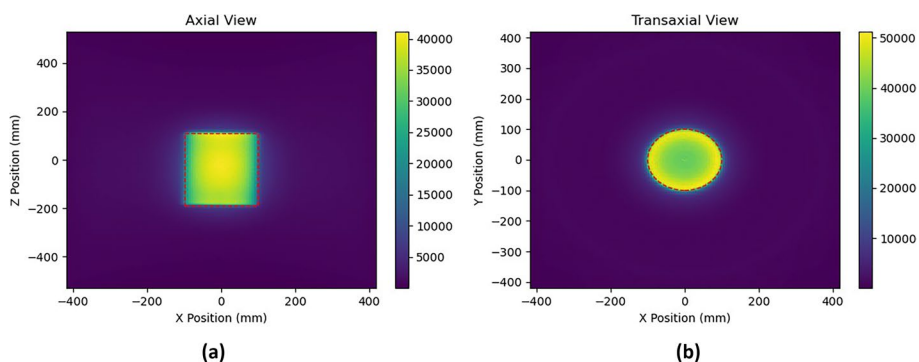
Fig. 4 Histo-images of the axial view summed over all Y planes (**a**) and transaxial view summed over all Z planes (**b**) of a uniform cylinder (20 $\phi \times$ 30 cm^3) filled with 16.3 MBq of ^{18}F. The dashed red lines denote the region of interest for extracting Ps lifetime information
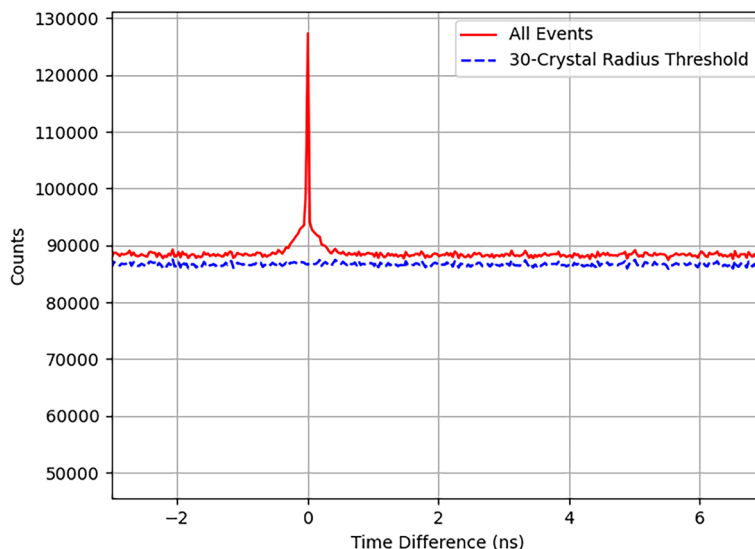
Fig. 5 Time-difference distribution produced from the ROI denoted in Fig. 4 with all events and with a 30-crystal distance threshold applied to the prompt gamma ray and annihilation photon interactions

cylinder with a defined region of interest (ROI) for extracting the positronium lifetime information. ^{18}F does not emit a prompt gamma ray and should produce a constant time-difference distribution. The solid red line in Fig. 5 shows the extracted time-difference distribution with a spike at $\Delta T_{Ps} = 0$.

The scintillator used in Quadra is LSO, which has a natural background due to ^{176}Lu. Figure 6 shows the ^{176}Lu decay scheme [24]

The three primary gamma rays emitted by ^{176}Lu have the following energies: 306.8 keV (γ_2), 201.8 keV (γ_3) and 88.4 keV (γ_4). The primary beta decay that has an endpoint energy of 595.8 keV along with the 88.4 keV gamma ray are not likely to escape the LSO. The 306.8 and 201.8 keV gamma rays do have a higher probability of escaping the crystal and interacting in neighboring crystals or detectors. The combined energy of these two gamma rays is also equal to 508.6 keV, which is indistinguishable in the scanner from a 511 keV annihilation photon. This series of interactions with energy broadening due to the resolution of the scintillator contains sufficient energy
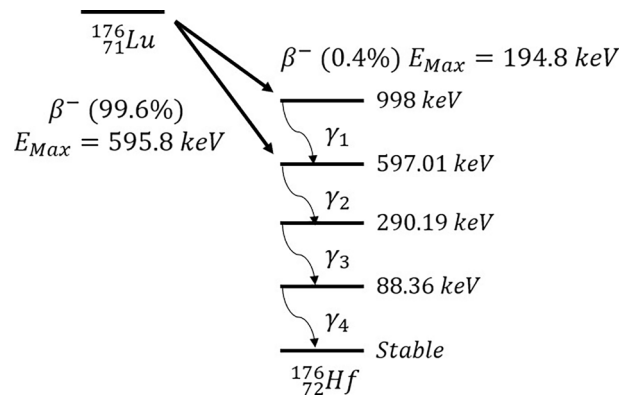
Fig. 6 Decay scheme for ^{176}Lu
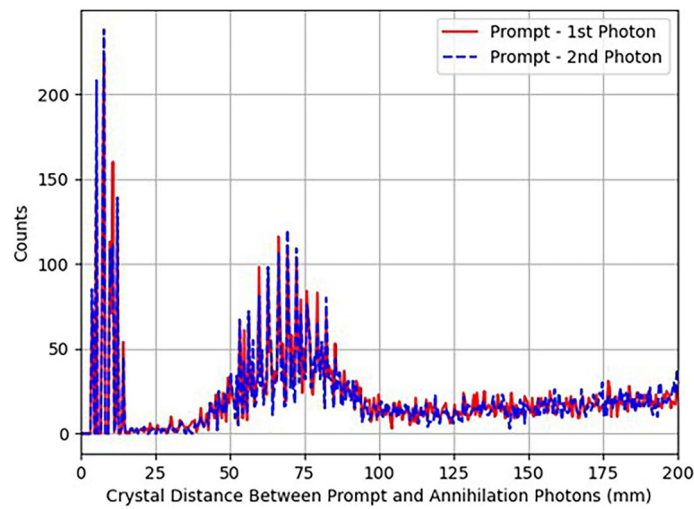
Fig. 7 The distance between the prompt gamma-ray interaction, $\vec{x_p}$, and either annihilation photon interaction, $\vec{x_0}$ or $\vec{x_1}$, in space assuming an 8 mm depth of interaction within a crystal for interactions with a time difference between −0.025 and 0.025 ns. Data is shown where the prompt gamma ray is the first photon detected (red) and where the prompt gamma ray is the second photon detected (blue) to visualize if there was a difference between the two types of series of interactions

to produce a fake prompt gamma ray and annihilation photon signal. This fake signal then only needs to be in coincidence with one true annihilation photon to appear as a triple-coincident event. The fake signal due to the ^{176}Lu background, however, are correlated in space and can be taken into account. Figure 7 shows the distribution of distances between the prompt gamma ray and a given annihilation photon interaction. There are two clear patterns in the data for interactions occurring at a distance of less than 10 mm and interactions occurring between 30 and 100 mm. Applying a threshold requiring the distance between the prompt gamma ray and a given annihilation photon to be greater than 30 crystals away, which is approximately a 100 mm radius threshold, yields the dashed blue line shown in Fig. 5. There is a slight decrease in efficiency of the system due to this threshold, however, it removes the contribution from the ^{176}Lu.

Fitting time-difference distributions

Double-exponential fit distribution

We consider three different fitting methodologies to determine the o-Ps lifetime. For the first methodology, the resulting net TDDs were fit starting from the maximum point with the following double exponential equation:

$$F(t) = Ae^{-\frac{t}{\tau_1}} + Be^{-\frac{t}{\tau_3}} + C, \tag{5}$$

where A, B and C are fit parameters and τ_1 and τ_3 are the pPs and oPs lifetimes. The fitting procedure is a frequentist non-linear fit that minimizes the χ^2 cost function and the parameters' errors are estimated from the diagonal elements of the covariance matrix.

Exponentially-modified gaussian distribution

The model in Equation (5) does not capture the contribution to the TDD from the direct annihilation of the positron, i.e. without forming a Ps state, nor any effects from the finite time resolution of the measurement apparatus. We therefore also modelled the measured TDD as a sum of three exponential components convolved with a normalized Gaussian function, i.e.

$$F(t) \; = \; b + N \cdot \sum_{i=1}^{3} BR_i \cdot \int_{-\infty}^{\infty} du \, \frac{e^{-u/\tau_i}\theta(u)}{\tau_i} \frac{e^{-(t-u-\Delta)^2/(2\sigma^2)}}{\sqrt{2\pi}\sigma}. \tag{6}$$

b denotes the background and N is a normalization constant which ensures that the relative intensities BR_i are a two-dimensional simplex, i.e. $\sum_{i=1}^{3} BR_i = 1$ for $BR_i \in [0,1]$. We identify the lifetime-intensity pairs (τ_1, BR_1) with the pPs, (τ_2, BR_2) with the direct annihilation and (τ_3, BR_3) with the oPs lifetime component, respectively. The two parameters Δ and σ characterize the mean and standard deviation of the Gaussian function that models the measurement process. The integral in Equation (6) can be rewritten in terms of the complementary error function erfc

$$F(t) \; = \; b + N \cdot \sum_{i=1}^{3} \frac{BR_i}{2\tau_i} e^{(\sigma^2 - 2t\tau_i + 2\Delta\,\tau_i)/(2\tau_i^2)} \cdot \text{erfc}\left(\frac{\sigma}{\sqrt{2}\tau_i} + \frac{\Delta - t}{\sqrt{2}\sigma} \right). \tag{7}$$

In this model, we neglect any additional time resolution functions or lifetime components as well as processes that happen on short time scales compared to ns like e.g. the positron thermalization.

   We used a Bayesian method to perform the fit of the model function in Equation (7) to the measured TDD. This method is described in the following section.

Bayes fit

The non-linear fitting procedure of the TDDs is not straight forward and involves several subtleties in the case of a frequentist fit [25–27].

   References [28, 29] highlight the advantages of a Bayesian inference for positronium lifetime spectra.

Our setup is as follows. The background, b, in Equation (6) is fixed by the median value of all measured time differences that are smaller than $-2\,\text{ns}$. Furthermore, we fix the p-Ps lifetime to $\tau_1 = 0.125\,\text{ns}$ and the direct annihilation time to $\tau_2 = 0.388\,\text{ns}$. The free fitting parameters are therefore the o-Ps lifetime τ_3, the three intensities $BR_{1,2,3}$ and the time resolution parameters σ and Δ. The prior distributions and parameters are

$$
\begin{aligned}
\tau_3 &\sim \mathcal{N}(1.5\,\text{ns}, 0.5\,\text{ns}), \\
BR_{1,2,3} &\sim \text{Dirichlet}(0.75, 3.1, 1.15), \\
\sigma &\sim \mathcal{N}(0.1\,\text{ns}, 0.05\,\text{ns}), \\
\Delta &\sim \mathcal{N}(0.0\,\text{ns}, 0.5\,\text{ns}).
\end{aligned}
\tag{8}
$$

The normal distributions for τ_3 and σ are truncated at zero. The three parameters of the Dirichlet distribution are chosen such that the expectation values for the intensities $BR_{1,2,3}$ are 0.15, 0.62 and 0.23 and the variances are 0.021, 0.039 and 0.030.

Then we assume a Gaussian likelihood. We refrain from considering a Poisson likelihood since the counting statistics of the triple events grossly underestimates the systematic error of the measurement.

The implementation of the Bayesian fit relies on the software packages described in References [30–32]. The posterior distributions are sampled using a no-u-turn algorithm [33] in order to avoid the dependence on the user defined step size and length of a standard Hamiltonian Monte Carlo algorithm. We use 12 chains with 5000 samples each, which is sufficient to reach numerical stability and convergence (see supplemental Figure 19).

As shown in Fig. 15 within the Results Section, the marginalized posterior distributions of $BR_{1,2,3}$ are bell-shaped. Therefore, it is meaningful to use a standard estimator for variance of BR_i. However, this is not generalizable and depends crucially on the noise in the measurement data. If e.g. the posterior distributions of $BR_{1,2,3}$ are reminiscent of a Dirichlet distribution, the variances should be computed accordingly. In this case a standard estimator would underestimate the variance significantly. We therefore quote the 68% highest density intervals (HDI) of the parameters' posterior distributions in analogy to the interval around the mean of two standard deviations in a normal distribution.

Experiments

Disk measurements

Two 10-μCi ^{22}Na positron sources were acquired from Spectrum Techniques. These sources have an Al/mylar window that is 0.0254 mm thick to allow positrons emitted by the ^{22}Na to escape the source. A drawing of the source is contained in the Supplementary Materials Section. These sources were measured independently and surrounded by quartz-glass and polycarbonate samples as shown in Fig. 8. The quartz glass (25.4 $\phi \times 5$ mm^3) samples were acquired from UQG Optics and the polycarbonate (10 $\phi \times 5$ mm^3) were acquired from EMCO Plastics. Seven independent measurements of the quartz-glass and six independent measurements of the polycarbonate samples were acquired for 15 min each. The background Ps lifetime from the positron sources were subtracted from the measurements with the samples. Special care was
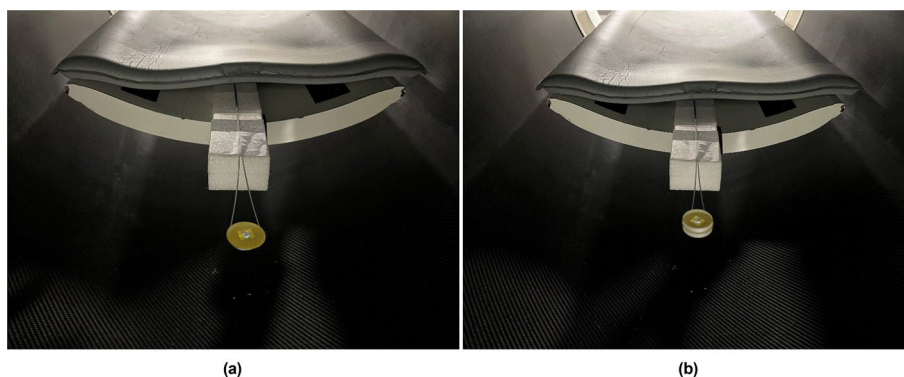
Fig. 8 Photographs of an experiment used to measure the o-Ps lifetime of quartz-glass samples using the [22]Na sources from Spectrum Techniques. The [22]Na sources were suspended on a wire and measured by themselves (**a**). The quartz-glass samples were then placed around the [22]Na sources to measure the o-Ps lifetime of the quartz glass (**b**)

Fig. 9 Photographs of an experiment used to measure the quartz-glass o-Ps lifetime using [68]Ga. Drops of the ^{68}Ga solution were placed on each disk shown in (**a**). Another disk of the same material was then placed on top and the two disks were taped together as shown in (**b**)

taken to ensure that the sources were in the same location in space for each measurement such that the source background could be accurately subtracted.

A similar experiment was performed using the quartz glass for the clinical radioisotopes. Figure 9 shows photographs of the setup that was used to measure the quartz-glass samples using the ^{68}Ga solution (eluate from a GalliPharm [68]Ge/^{68}Ga generator, Eckert & Ziegler Radiopharma GmbH). Drops of the solution were placed on top of each disk shown in Fig. 9a. An additional disk of the same material was then placed on top and taped down as shown in Fig. 9b. Data were acquired for one hour for this measurement using a ^{68}Ga solution with approximately 5 MBq placed in between the samples. The resulting histo-image of the measurement is shown in Fig. 10. A spherical volume of interest was set around the quartz-glass sample to analyze the resulting Ps lifetime distribution.

A similar setup was used for the [82]Rb (chloride solution from a CardioGen-82 [82]Sr/[82]Rb generator, Bracco Diagnostics Inc.) and [124]I measurements (sodium iodine solution from DSD Pharma GmbH). Data were acquired from both measurements for 10 min. The infused activity present at end of elution for the [82]Rb solution was 670.91 MBq in a volume of 50 ml. Only about a milliliter was placed between the quartz glass, which gave an initial activity of approximately 13 MBq. An activity of 4.7
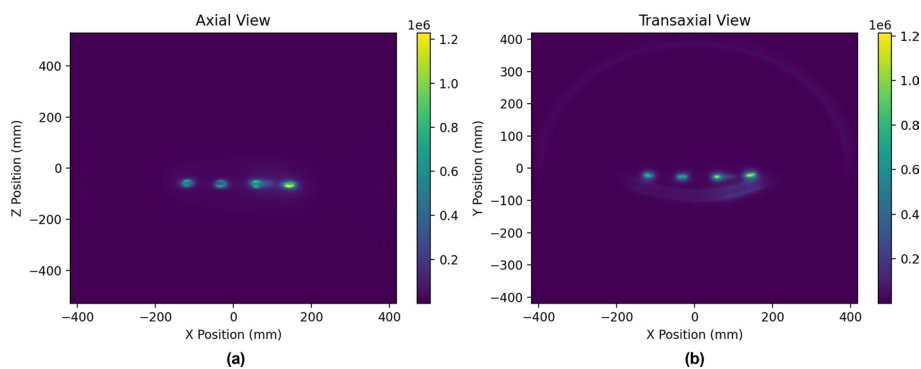
Fig. 10 Histo-images of the axial view summed over all Y planes (**a**) and transaxial view summed over all Z planes (**b**) of the measurement shown in Fig. 9

MBq was distributed between the disks for the ^{124}I measurement. It should be noted, however, that there was some spilling when performing the ^{124}I measurement. We estimate an activity of 1 MBq between the quartz disks for the ^{124}I measurement. The lifetimes from the metal disks are not assessed in this manuscript.

^{82}Rb uniform-cylinder measurement

A water-filled uniform cylinder (20 $\phi \times$ 30 cm^3) with a ^{82}Rb solution (initial activity of approximately 73.3 MBq and 20 ml) was measured for 10 min. The cylinder was filled with demineralized water and the ^{82}Rb solution. The ^{82}Rb solution added 0.9% NaCl concentration to the water. Data were processed to extract the o-Ps lifetime for water and assess the impact of scatter and attenuation on the resulting TDDs.

Results

^{22}Na positron source

Data acquired using the ^{22}Na positron sources was processed using the above methodology. Spherical volumes of interest were set with a 15 mm radius around the source location and time-difference values were acquired from the defined region. For this series of measurements, the positron source was measured by itself and then placed between the quartz-glass and polycarbonate samples. The positron source was measured by itself to be able to subtract the inherent Ps lifetime and generate net time-difference spectra for each sample. The drawing of the ^{22}Na source contained in the Supplementary Materials Section shows that the ^{22}Na salt is deposited on a plastic laminate disk that is approximately 0.5 mm thick. Two of these sources were used for these measurements, which means that there is approximately an additional millimeter of plastic material that will have its own respective o-Ps lifetime. This lifetime of the source itself must be subtracted out to measure the lifetimes of only the quartz glass and polycarbonate. Figure 11 shows the measured lifetime of the quartz-glass samples with the ^{22}Na sources, the lifetime spectrum produced from the ^{22}Na sources themselves and the net quartz-glass spectrum. Figure 11 shows that the lifetime contribution from the ^{22}Na sources is non negligible.

Figure 12 shows net time-difference spectra for one of the quartz-glass and polycarbonate measurements. Seven independent measurements were performed for the
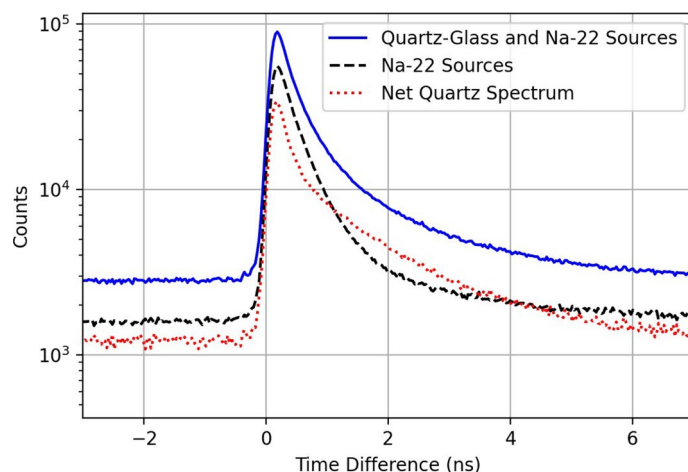
Fig. 11 Measured lifetime spectrum of the quartz-glass samples with the ^{22}Na sources, the measured lifetime spectrum produced from the ^{22}Na sources themselves and the net quartz-glass spectrum
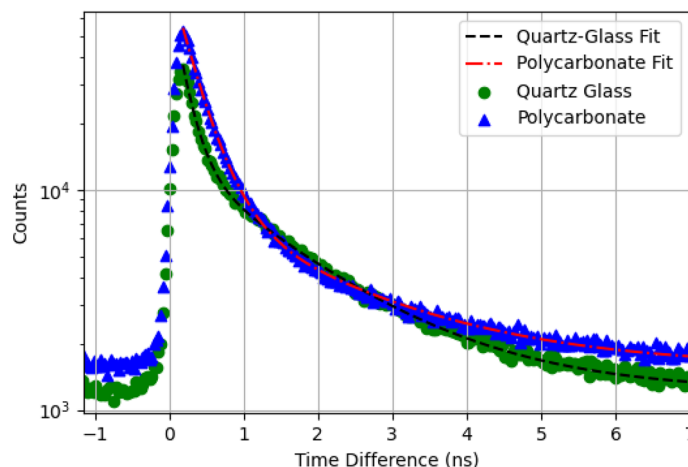
Fig. 12 Net time-difference spectra for the quartz glass and polycarbonate measurements with a ^{22}Na source. Fits are shown using Eq. (5)

quartz-glass sample and six independent measurements were performed for the polycarbonate samples. Each of the resulting net time-difference spectra were fit with Eq. (5) after the peak of the distribution to estimate the o-Ps lifetime. Results produced o-Ps lifetimes of 1.538 ± 0.036 ns for the quartz glass and 1.927 ± 0.042 ns for the polycarbonate where the uncertainty is a single standard deviation from the seven and six independent measurements of the quartz-glass and polycarbonate measurements respectively.

Quartz-glass ps lifetime comparisons

The quartz-glass samples were additionally measured with the following radioisotopes: ^{68}Ga, ^{82}Rb and ^{124}I. The methodology detailed above was applied to the collected data, and spherical volumes of interest were set with a 15 mm radius around each of the quartz-glass samples to extract the time-difference spectra. Figure 13
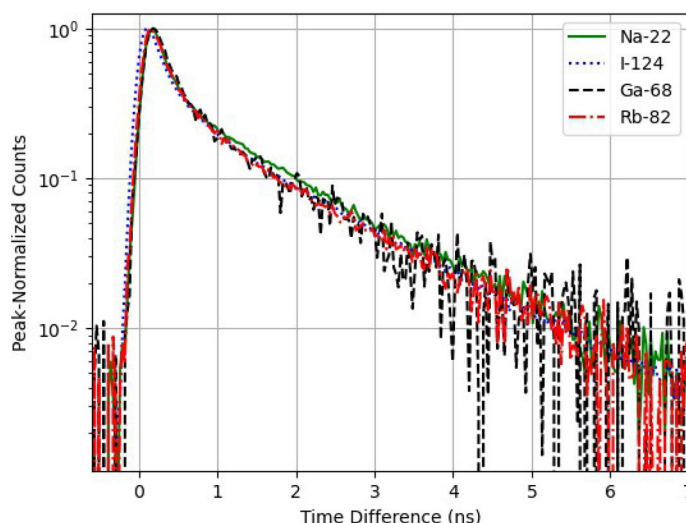
Fig. 13 Time-difference spectra measured for a quartz-glass sample using four radioisotopes that emit a prompt gamma ray
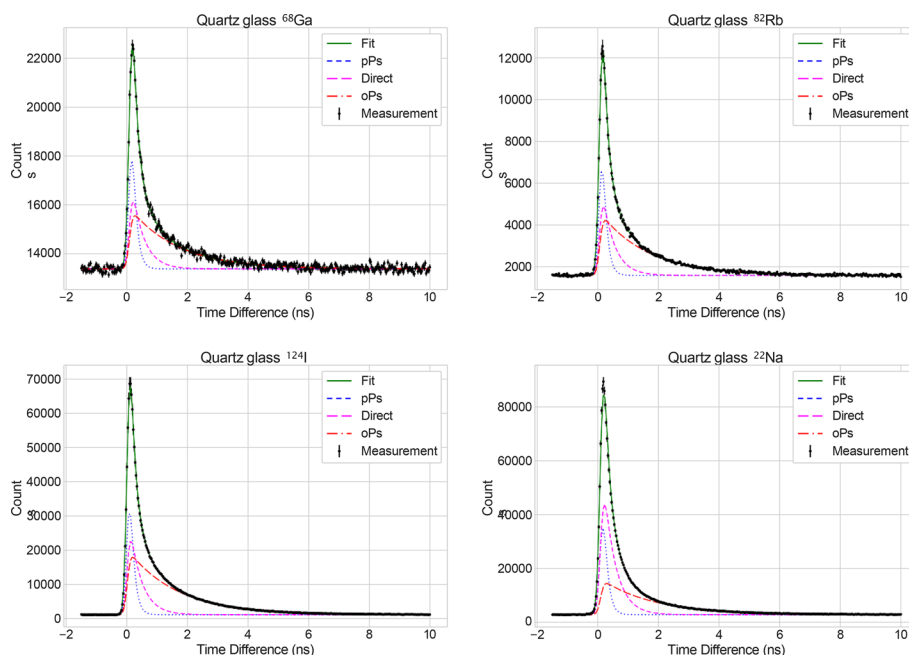
Fig. 14 Bayes fit using Eq. (7) to quartz glass data with the contributions of the Ps lifetime components

shows a peak-normalized comparison between the four source measurements and Fig. 14 shows the resulting fits to the TDDs. Each of these resulting time-difference spectra were fit with the exponentially-modified Gaussian distributions using the Bayesian methodology detailed in the Bayes Fit section. The resulting fit parameters are detailed in Table 1. Figure 15 shows an example of the pair plot of the posterior distributions for the parameters τ_3, BR_3, σ and Δ for the ^{124}I quartz-glass data.

Table 1 Mean and 68% HDI interval of the Bayes fit for the quartz glass data. The values for the background b and normalization factor N are not shown due to their marginal relevance

Isotope	τ_3 [ns]	BR_1	BR_2	BR_3	Isotope	σ [ns]	Δ [ns]
^{124}I	1.624 [1.618, 1.632]	0.178 [0.171, 0.185]	0.237 [0.229, 0.246]	0.585 [0.581, 0.589]	^{124}I	0.085 [0.084, 0.086]	0.016 [0.015, 0.018]
^{68}Ga	1.584 [1.514, 1.648]	0.203 [0.189, 0.216]	0.233 [0.209, 0.261]	0.564 [0.549, 0.578]	^{68}Ga	0.089 [0.087, 0.091]	0.088 [0.086, 0.090]
^{82}Rb	1.589 [1.564, 1.614]	0.191 [0.181, 0.200]	0.234 [0.220, 0.249]	0.575 [0.568, 0.582]	^{82}Rb	0.087 [0.086, 0.088]	0.064 [0.062, 0.067]
^{22}Na	1.739 [1.729, 1.750]	0.182 [0.176, 0.187]	0.424 [0.418, 0.431]	0.394 [0.392, 0.397]	^{22}Na	0.094 [0.093, 0.095]	0.093 [0.091, 0.094]
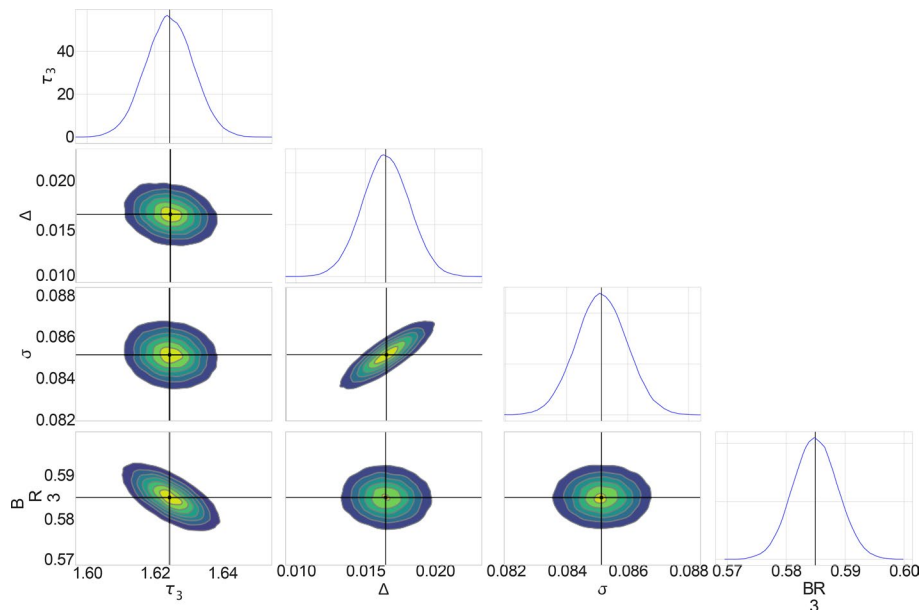
Fig. 15 Pair plot of the posterior distributions for the parameters τ_3, BR_3, σ and Δ for the ^{124}I quartz glass data

^{82}Rb Uniform cylinder measurement

The water-filled uniform cylinder with an added ^{82}Rb solution was measured and data were processed using the detailed methodology. Time-difference data were extracted from the following volumes of interest within the cylinder: (5 $\phi \times$ 15 cm^3), (10 $\phi \times$ 20 cm^3) and (15 ϕ $\times$ 25 cm^3). Figure 16 shows the generated histo-images from the uniform cylinder measurement with the volumes of interest shown as the dashed red lines. The resulting time-difference spectra are shown in Fig. 17, which compares the results from the cylinder with the quartz-glass distribution measured using ^{82}Rb shown in Fig. 13. Each of the distributions from the uniform cylinder were fit with the exponentially-modified Gaussian distributions using the Bayesian methodology. The resulting fits are shown in Fig. 18. The fit parameters are contained in Table 2.
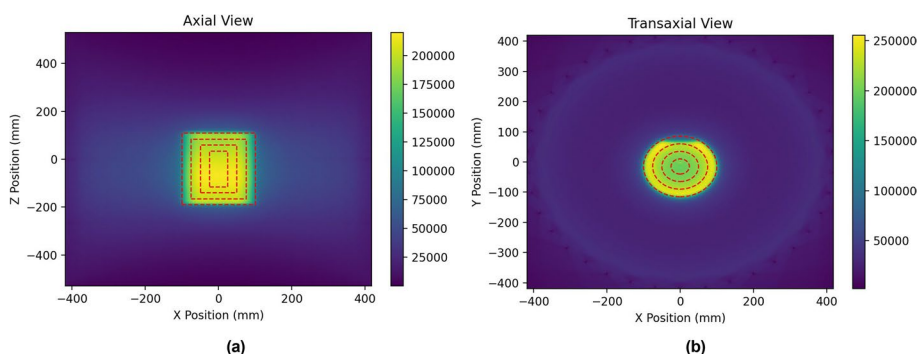
Fig. 16 Histo-images of the axial view summed over all Y planes (**a**) and transaxial view summed over all Z planes (**b**) of a uniform cylinder filled with an estimated initial activity of 73.3 MBq of ^{82}Rb. The dashed red lines denote the regions of interest for extracting Ps lifetime information
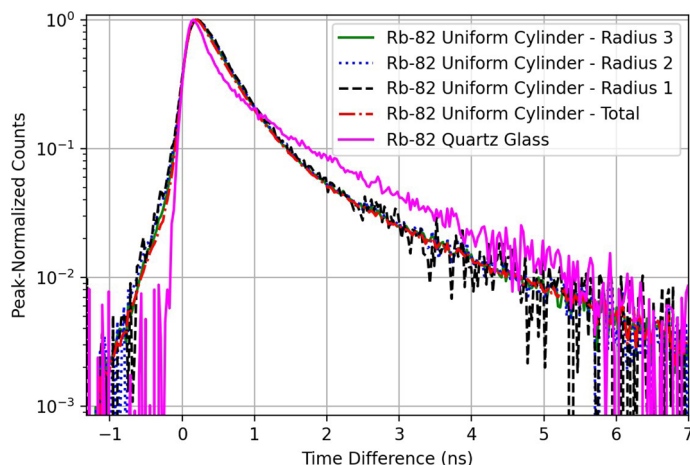
Fig. 17 Comparison of the time-difference spectra extracted from the uniform cylinder shown in Fig. 16 with the quartz-glass sample measured using ^{82}Rb. The various radii data are from the smallest to largest radii as shown in Fig. 16

Discussion

Comparing Quartz-Glass o-Ps lifetime results

Results detailed by Takyu et al. [16] and Shibuya et al. [12] fit a specific region of the time-difference spectra extracted from the various measurements with an exponential distribution to extract the o-Ps lifetime. Takyu et al. found the lifetimes for the quartz-glass and polycarbonate samples to be 1.56 ± 0.08 and 2.07 ± 0.16 ns respectively. Results in this work found the values to be 1.538 ± 0.036 ns for the quartz glass and 1.927 ± 0.042 ns for the polycarbonate. These results are within a single standard deviation and agree well. Figure 13, however, shows a limitation for these types of measurements. Visually, the green curve produced from the ^{22}Na measurement does not agree with the other curves in the 1–3 ns region of the distribution. While this difference does not seem significant, applying the exponentially-modified Gaussian distribution with the Bayesian fitting methodology results in an o-Ps lifetime that is measurably larger than the lifetimes measured with the other sources: 1.74 ± 0.01 for ^{22}Na, 1.59 ± 0.03 ns for ^{82}Rb, 1.58 ± 0.07 ns for ^{68}Ga and 1.62 ± 0.01 ns for ^{124}I. The results for all the isotopes
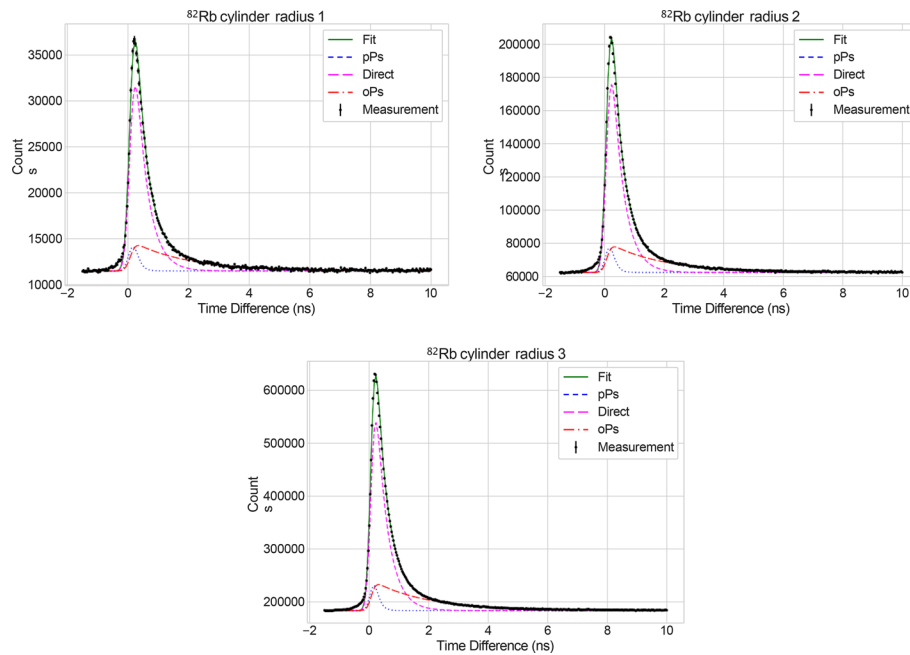
Fig. 18 Bayesian fit result for the homogeneous ^{82}Rb cylinder with the three lifetime components

Table 2 Mean and 68% HDI interval of the Bayes fit for the homogeneous cylinder filled with ^{82}Rb. The values for the background b and normalization factor N are not shown due to their marginal relevance

Isotope	τ_3 [ns]	BR_1	BR_2	BR_3
^{82}Rb radius 1	1.819 [1.764, 1.871]	0.053 [0.042, 0.064]	0.663 [0.648, 0.676]	0.285 [0.28, 0.289]
^{82}Rb radius 2	1.812 [1.787, 1.835]	0.052 [0.047, 0.057]	0.662 [0.656, 0.668]	0.286 [0.284, 0.288]
^{82}Rb radius 3	1.815 [1.803, 1.828]	0.051 [0.049, 0.054]	0.656 [0.653, 0.659]	0.293 [0.292, 0.294]

Isotope	σ [ns]	Δ [ns]		
^{82}Rb radius 1	0.136 [0.134, 0.137]	0.080 [0.078, 0.083]		
^{82}Rb radius 2	0.128 [0.127, 0.128]	0.078 [0.077, 0.079]		
^{82}Rb radius 3	0.119 [0.118, 0.119]	0.075 [0.074, 0.075]		

with the exception of ^{22}Na agree with Takyu et al. [16] and Van Horn et al. who measured the o-Ps lifetime for quartz glass to be 1.607 ± 0.006 ns [34]. The analysis reported by Van Horn et al. detailed different values for τ_1 and τ_2 relative to the assumed values presented in this manuscript where $\tau_1 = 0.125$ ns and $\tau_2 = 0.388$ ns. The resulting o-Ps lifetime, however, does not seem to be significantly impacted. This result aligns well with results from Kotera et al. who showed that the o-Ps lifetime, τ_3, only has a small correlation with I_1 or BR_1 as designated in this manuscript [4]. For the ^{22}Na measurements, it was assumed that scatter and attenuation from the quartz-glass sample would not suppress the intensity of the source itself such that the inherent Ps lifetime spectrum from the ^{22}Na source could be accurately subtracted to extract a net time-difference spectrum for the quartz glass. This explanation is one possibility for the difference in measured

lifetimes. Additionally, it is possible that positrons that escape the ^{22}Na source thermalize and scatter back into the source itself to form Ps. This additional effect may also explain the shape difference. These effects are not a significant contribution to the clinical isotopes because only a small drop of solution was placed between the quartz-glass samples. It was assumed that the thin layer of solution formed would have a negligible impact on the measurement. Each of the results from the clinical radioisotopes are within a single standard deviation of each other and the magnitude of the uncertainty reported is directly related to the number of acquired counts due to the source being measured. It should be noted that the ^{68}Ga spectrum has a higher level of noise compared to the other spectra. There are two reasons for this result. The first is that the branching ratio of ^{68}Ga, 3.23%, is much lower than the other isotopes. The second is that the prompt gamma ray is outside of the dynamic range of the detectors. It is estimated that the system can measure events up to 950 keV while the energy of the prompt gamma ray for ^{68}Ga is 1077.3 keV. This limitation means that a significant portion of the prompt gamma rays from ^{68}Ga will not be detected, which decreases the signal from this source.

Uniform cylinder measurement

Figure 17 shows a direct comparison of the time-difference spectra between the volumes of interest specified in Fig. 16 with the quartz-glass measurement using ^{82}Rb. The first notable result from Fig. 17 is that there is no significant shape change in the time-difference spectra between the specified volumes of interest within the uniform cylinder. There is, however, still an effect due to the scatter within the uniform cylinder. Visually, it can be seen that there is a higher intensity in the regions from −1 to 0 ns and 0.5 to 1 ns for the uniform cylinder spectra relative to the quartz-glass spectrum. It is assumed that this intensity difference within these regions is due to scattering of the photons in the measurement that is generating this broadening in the prompt peak. Past about 1 ns in the distribution, the o-Ps lifetime appears to still dominate the spectra. Results from the fitting yielded an o-Ps lifetime of 1.815 ± 0.013 ns, which agrees well with the result detailed by Kotera et al. and Stepanov et al. [4, 35]. Kotera et al. found the o-Ps lifetime of water to be 1.839 ± 0.015 ns at 20 °C [4] and Stepanov et al. found the o-Ps lifetime of water to be 1.802 ± 0.015 ns. It should be noted that the temperature of the uniform cylinder was not recorded and the added salt from the ^{82}Rb solution may be responsible for the slight difference between the lifetime results. Kotera et al. also found that the o-Ps lifetime is not significantly dependent on the intensities of the other lifetime components or the values of the direct annihilation lifetime or the p-Ps lifetime. It is possible that because the o-Ps lifetime is not significantly correlated with these other parameters such that the o-Ps lifetime value can still be accurately extracted even with a significant scatter volume that is changing the shape of the prompt peak. This result is subtly different than the result discussed in the previous section discussing the quartz results. The difference being the accurate subtraction of the ^{22}Na source compared with no measurement change for the uniform cylinder. It will be of interest, however, to perform additional measurements with various volumes of scatter medium to validate these assumptions regarding the impact of scatter on the o-Ps lifetime experimentally.

Conclusion

The results presented in this manuscript detail two independent series of measurements that produced o-Ps lifetimes that agree with previously published results. The o-Ps lifetime for quartz-glass and polycarbonate samples using a ^{22}Na positron source were measured to be 1.538 $\pm$ 0.036 ns for the quartz glass and 1.927 $\pm$ 0.042 ns for the polycarbonate. In addition, a water-filled uniform cylinder with a ^{82}Rb solution yielded an o-Ps lifetime for water of 1.815 $\pm$ 0.013 ns, which also agrees with previously published data. The agreement of these results validate the proposed methodology and capability of the Quadra scanner to perform positronium lifetime imaging.

Abbreviations

Ps	Positronium
p-Ps	Para-positronium
o-Ps	Ortho-positronium
PET	Positron emission tomography
Quadra	Biograph vision quadra (Siemens Healthineers)
LA-FOV	Long-axial field-of-view
TDD	Time-difference distribution
ROI	Region of interest
HDI	Highest density interval

Supplementary Information

The online version contains supplementary material available at https://doi.org/10.1186/s40658-024-00678-4.

> Supplementary Material 1.

Author contributions

W.M.S. made the following contributions to the manuscript: corresponding author, primary writer, planned and participated in experiments, wrote the list-mode processing software and analyzed the data. L.M. made the following contributions to the manuscript: primary writer, planned and participated in experiments, wrote the fitting algorithms and analyzed the data. J.B. supported analyzing and interpreting the data for the ^{176}Lu background contribution. H.S. coordinated, planned and participated in the experiments, and was key to the licensing of software for data acquisition from Quadra. S.P., S.W.N., G.L., P.M., E.S., A.R., K.S. and M.C. all helped in some capacity for coordinating, planning and/or executing the experiments as well as understanding the results. All authors read and approved the final manuscript.

Availability of data and materials

The list-mode data and source code cannot be made available, but the functionality was implemented in a software prototype that can be shared under the terms of a software license agreement. Net images and resulting TDDs presented in this manuscript, however, have been made available on Zenodo with the https://doi.org/10.5281/zenodo.12636019. Additional data can be made availble upon reasonable request.

Declarations

Ethics approval and consent to participate

Not applicable.

Consent for publication

Not applicable.

Competing interest

W.M.S, J.B., H.S. and M.C. are employees of Siemens Medical Solutions USA, Inc., and Siemens Healthineers International AG. P. M. is an inventor on a patent related to this work. Patent nos.: (Poland) PL 227658, (Europe) EP 3039453, and (United States) US 9,851,456], filed (Poland) 30 August 2013, (Europe) 29 August 2014, and (United States) 29 August 2014; published (Poland) 23 January 2018, (Europe) 29 April 2020, and (United States) 26 December 2017. A.R. has

References

1. Bass SD, Mariazzi S, Moskal P, Stępień E. Colloquium: positronium physics and biomedical applications. Rev Modern Phys. 2023;95(2): 021002.
2. Charlton MJ. Positron physics. Cambridge Monographs on Atomic, Molecular and Chemical Physics. Cambridge: The Press Syndicate of the University of Cambridge; 2001.
3. Weisberg H, Berko S. Positron lifetimes in metals. Phys Rev. 1967;154(2):249. https://doi.org/10.1103/PhysRev.154. 249.
4. Kotera K, Saito T, Yamanaka T. Measurement of positron lifetime to probe the mixed molecular states of liquid water. Phys Lett A. 2005;345(1−3):184−90. https://doi.org/10.1016/j.physleta.2005.07.018.
5. Trung NT, Duong NT, Hien NQ, Tap TD, Thanh ND. Investigation of ortho-positronium annihilation for porous materials with different geometries and topologies. Sci Rep. 2023;13(1):13707. https://doi.org/10.1038/s41598-023-40901-3.
6. Murtagh DJ, Cooke DA, Laricchia G. Excited-state positronium formation from helium, argon, and xenon. Phys Rev Lett. 2009;102(13): 133202. https://doi.org/10.1103/PhysRevLett.102.133202.
7. Moskal P, Jasińska B, Stępień EŁ, Bass SD. Positronium in medicine and biology. Nat Rev Phys. 2019;1(9):527−9.
8. Champion C, Le Loirec C. Positron follow-up in liquid water: II. Spatial and energetic study for the most important radioisotopes used in pet. Phys Med Biol. 2007;55:6605.
9. Stepanov SV, Byakov VM, Stepanov PS. Positronium in biosystems and medicine: a new approach to tumor diagnostics based on correlation between oxygenation of tissues and lifetime of the positronium atom. Phys Wave Phenom. 2021;29(2):174−9. https://doi.org/10.3103/S1541308X21020138.
10. Moskal P, et al. Feasibility study of the positronium imaging with the j-pet tomograph. Phys Med Biol. 2019;64: 055017. https://doi.org/10.1088/1361-6560/aafe20.
11. Moskal P, et al. Positronium imaging with the novel multiphoton pet scanner. Sci Adv. 2021;7: eabh4394. https://doi.org/10.1126/sciadv.abh4394.
12. Shibuya K, Saito H, Nishikido F, Takahashi M, Yamaya T. Oxygen sensing ability of positronium atom for tumor hypoxia imaging. Commun Phys. 2020. https://doi.org/10.1038/s42005-020-00440-z.
13. Moskal P, et al. Developing a novel positronium biomarker for cardiac myxoma imaging. EJNMMI Phys. 2023;10:22. https://doi.org/10.1186/s40658-023-00543-w.
14. Qi J, Huang B. Positronium lifetime image reconstruction for Tof pet. IEEE Trans Med Imaging. 2022;41(10):2848−55. https://doi.org/10.1109/TMI.2022.3174561.
15. Huang B, Li T. Split: statistical positronium lifetime image reconstruction via time-thresholding. IEEE Trans Med Imaging. 2024. https://doi.org/10.1109/TMI.2024.3357659.
16. Takyu S, Shibuya K, Nishikido F, Tashima H, Takahashi M, Yamaya T. Two-dimensional positronium lifetime imaging using certified reference materials. Appl Phys Exp. 2022;15(10): 106001. https://doi.org/10.35848/1882-0786/ac8d7b.
17. Moskal P et al. First positronium image of the human brain in vivo.
18. Moskal P, et al. Performance assessment of the 2 positronium imaging with the total-body pet scanners. EJNMMI Phys. 2020;7:1−16.
19. Jasińska B et al. Human tissues investigation using pals technique. Med Phys 2017; https://doi.org/10.48550/arXiv.1711.04512.
20. Jasińska B, Moskal P. A new pet diagnostic indicator based on the ratio of 3gamma/2gamma positron annihilation. Acta Phys Polon B 2017.
21. Moskal PES, Moskal P, Stępień EŁ. Positronium as a biomarker of hypoxia. Bio-Algor Med-Syst. 2022;17(4):311−9.
22. Prenosil GA, Sari H, Fürstner M, Afshar-Oromieh A, Shi K, Rominger A, Hentschel M. Performance characteristics of the Biograph Vision Quadra PET/CT system with a long axial field of view using the NEMA NU 2−2018 standard. J Nucl Med. 2022;63(3):476−84.
23. Takyu S et al. Initial demonstration of quantum pet: 2d positronium lifetime imaging using a pair of tof detectors. In: Virtual IEEE Nuclear Science Symposium and Medical Imaging Conference 2021.
24. Rothfuss H, Panin V, Casey M. LSO background radiation as a transmission source using time of flight. Phys Med Biol. 2014;59(18):5483. https://doi.org/10.1088/0031-9155/59/18/5483.
25. Dulski K. Pals avalanche: a new pal spectra analysis software. Acta Phys Polon A. 2020. https://doi.org/10.12693/APhysPolA.137.167.
26. Olsen JV, Kirkegaard P, Pedersen NJ, Eldrup M. PALSfit: a new program for the evaluation of positron lifetime spectra. Phys Status Solidi C. 2007;4:4004−6. https://doi.org/10.1002/pssc.200675868.
27. Olsen JV, Kirkegaard P, Eldrup M. Palsfit3: a software package for the analysis of positron lifetime spectra (edition 2022). 2022.
28. Gu B, Zhang W, Liu J, Zhang H, Ye B. Accurate and informative analysis of positron annihilation lifetime spectra by using Markov chain Monte-carlo Bayesian inference method. Nucl Instrum Methods Phys Res Sect A Accel Spectrom Detect Assoc Equip. 2019;928:37−42. https://doi.org/10.1016/j.nima.2019.02.056.
29. Pascual-Izarra C, et al. Advanced fitting algorithms for analysing positron annihilation lifetime spectra. Nucl Instrum Methods Phys Res Sect A Accel Spectrom Detect Assoc Equip. 2009;603:456−66. https://doi.org/10.1016/j.nima.2009.01.205.

30. Bezanson J, Edelman A, Karpinski S, Shah VB. Julia: a fresh approach to numerical computing. SIAM Rev. 2017;59:65–98.
31. Ge H, Xu K, Ghahramani Z. Turing: a language for flexible probabilistic inference. In International Conference on Artificial Intelligence and Statistics, AISTATS 2018, 9–11 April 2018, Playa Blanca, Lanzarote, Canary Islands, Spain, 2018;1682–1690.
32. Kumar R, Carroll C, Hartikainen A, Martin O. ArviZ a unified library for exploratory analysis of Bayesian models in python. J Open Source Softw. 2019;4:1143. https://doi.org/10.21105/joss.01143.
33. Hoffman MD, Gelman A, et al. The no-u-turn sampler: adaptively setting path lengths in Hamiltonian Monte Carlo. J Learn Res. 2014;15:1593–623 arXiv:1111.4246.
34. Van Horn JD, Wu F, Corsiglia G, Jean YC. Asymmetric positron interactions with chiral quartz crystals?. In Defect and Diffusion Forum 2016. https://doi.org/10.4028/www.scientific.net/DDF.373.221.
35. Stepanov PS, Selim FA, Stepanov SV, Bokov AV, Ilyukhina OV, Duplâtre G, Byakov VM. Interaction of positronium with dissolved oxygen in liquids. Phys Chem Chem Phys. 2020;22(9):5123–31. https://doi.org/10.1039/C9CP06105C.

Publisher's Note